doi:10.26443/seismica.v5i2.2576

SEISMICA

Crustal Thickness Variations Beneath the Western Indian Ocean Using Teleseismic P-Wave Coda Autocorrelations on Ocean-Bottom Seismic Data

Ali T S Saneesh * [1,2], **David Schlaphorst** [3,4], **Sandeep Gupta** [1,2]

[1]CSIR-National Geophysical Research Institute, Hyderabad 500007, India, [2]Academy of Scientific and Innovative Research (AcSIR), Ghaziabad 201002, India, [3]IDL - Instituto Dom Luiz, Universidade de Lisboa, Lisboa, Portugal, [4]Lisbon School of Engineering (ISEL), Lisbon, Portugal

Author contributions: *Conceptualization*: Ali T S Saneesh, David Schlaphorst. *Methodology*: Ali T S Saneesh, Sandeep Gupta. *Formal Analysis*: Ali T S Saneesh, David Schlaphorst, Sandeep Gupta. *Writing - Original draft*: Ali T S Saneesh. *Writing - Review & Editing*: Ali T S Saneesh, David Schlaphorst, Sandeep Gupta. *Supervision*: Sandeep Gupta.

Abstract The western Indian Ocean is a key region for investigating lithospheric evolution, as it records a complex interplay of tectonic, magmatic, and mantle processes. Constraining crustal thickness across this area is therefore essential for understanding how these processes interact and shape the region's geodynamic development. In this study, we apply teleseismic P-wave coda autocorrelation to map crustal thickness across the western Indian Ocean using data from 54 ocean-bottom seismometers (OBSs) and 7 land-based seismic stations. Our results reveal pronounced lateral variations in crustal thickness, ranging from ∼4.3 km beneath young oceanic crust near the Central Indian Ridge (CIR) to ∼25.85 km along the eastern margin of Madagascar. The oceanic domain exhibits a mean crustal thickness of ∼7.01 ± 0.27 km, consistent with global oceanic averages. Volcanic islands within the Mozambique Channel show crustal thicknesses between ∼11.21 and 23.98 km, whereas those in the Mascarene Basin display values of ∼10.73 km and ∼14.63 km. These localized zones of crustal thickening beneath volcanic islands likely reflect long-lived magmatic underplating and hotspot-related intrusions. Collectively, these findings provide new quantitative constraints on the tectono-magmatic processes that govern crustal formation, modification, and isostatic compensation in this geodynamically complex region.

Non-technical summary The western Indian Ocean (WIO) is an ideal region for understanding how the Earth's crust forms and evolves. This area includes oceanic crust, volcanic islands, and continental margins, all shaped by tectonic movements, volcanic activity, and deep mantle processes. However, the thickness of the crust beneath many parts of this region remains poorly understood, mainly because collecting geophysical data in the ocean is difficult. Estimating crustal thickness in this region is important because it helps us understand how ocean basins form and how volcanic islands develop. In this study, we used seismic waves from distant earthquakes recorded by 54 ocean-bottom seismometers and 7 land-based seismic stations. By analyzing the echoes of these waves within the Earth, we estimated crustal thickness across the WIO. Our results show that the crust is thin beneath young oceanic areas near the Central Indian Ridge, much thicker beneath Madagascar, and beneath volcanic islands. These thicker areas likely formed when magma was added to the base of, or inside, the crust over a long period. This study provides a regional map of crustal thickness for the WIO and helps improve our understanding of how tectonic and volcanic processes shape the seafloor and adjacent continental margins.

Production Editor: Gareth Funning
Handling Editor: Anant Hariharan
Copy & Layout Editor: Miriam Gauntlett

Signed reviewer(s): Guilhem Barruol, Thanh-Son Phạm

Received: 2026-01-30
Accepted: 2026-06-09
Published: 2026-07-03

1 Introduction

Understanding the geometry of the Mohorovičić discontinuity (Moho) is fundamental for constraining crustal thickness and structure. It provides key insights into lithospheric formation and evolution, the mechanisms of isostatic compensation, and the transfer of magmatic flux from the mantle to the crust (Steinhart, 1967). Despite considerable advances, many parts of the crustal structure remain poorly resolved, especially in many marine regions, owing to limited observational coverage. Passive seismology offers a robust framework for imaging subsurface structures using naturally occurring seismic signals; however, its application in oceanic settings is often limited by the availability of seismic stations rather than methodological limitations. Where sufficient data exist, passive seismic observations provide valuable constraints on crustal thickness and enable independent testing of isostatic models derived from surface topography (e.g., Kearey et al., 2009).

The western Indian Ocean (Fig. 1) provides an ideal setting for investigating crustal and upper-mantle structures, as it exhibits a complex interplay between tectonic plate motion, seafloor spreading, fracture zones, and mantle upwelling. This region encompasses the Central Indian Ridge (CIR), the Southwest Indian Ridge (SWIR), the Mascarene Basin, the Mozambique Basin,

*Corresponding author: contactsaneeshali@gmail.com

the Rodrigues Triple Junction (RTJ), and major fracture zones such as the Mauritius Fracture Zone (MauFZ), Mahanoro Fracture Zone (MhnFZ), and Southern Boussole Fracture Zone (SBFZ). These structures document a long history of plate reorganization and magmatic activity, spanning from the Late Cretaceous to the present (Lénat, 2015). Tectonically, the region is governed by the divergent boundary between the African and Indo-Australian plates, expressed as the CIR, a slow-to-intermediate spreading system connected to adjacent ridges through the RTJ (Fisher et al., 1971).

Our study utilizes earthquake data from the RHUM-RUM (Réunion Hotspot and Upper Mantle – Réunion Unterer Mantel) experiment (Barruol et al., 2017), a large-scale passive seismic deployment conducted from 2011 to 2015 around La Réunion, located in the Western Indian Ocean, ∼800 km east of Madagascar and ∼200 km southwest of Mauritius, together with a permanent GEOSCOPE station also located on La Réunion Island (Fig. 1). This region is volcanically active, with La Réunion's hotspot volcanism persisting since ∼65 Ma. Its age-progressive hotspot extends several thousand kilometers to the north, linking La Réunion to the Deccan Traps (∼3000–3500 km away) and the Seychelles (∼1800 km to the north), providing compelling evidence for a deep-rooted mantle plume beneath the island (Barruol and Sigloch, 2013; Owen-Smith et al., 2013). The RHUM-RUM project was designed to image mantle structure from crust to core in order to investigate this plume hypothesis (Barruol and Sigloch, 2013; Barruol et al., 2019; Tsekhmistrenko et al., 2021). Several geophysical studies based on this dataset have since provided important insights into the lithospheric and upper-mantle structure of the region. In particular, Rayleigh-wave tomography and ambient noise analyses have revealed marked lithospheric heterogeneity, expressed as variations in upper-mantle velocity, seismic anisotropy, and broad crustal structure linked to past and ongoing tectono-magmatic processes (e.g., Mazzullo et al., 2017; Hable et al., 2019). Receiver function studies have further provided valuable local constraints on crustal thickness in parts of the region (e.g., Fontaine et al., 2015; Dofal et al., 2021, 2023; Dofal, 2021), while broader-scale crustal thickness estimates have also been inferred from the CRUST1.0 reference model (Laske et al., 2013).

To investigate Moho geometry beneath the western Indian Ocean, we employ teleseismic P-wave coda autocorrelation. Although receiver function techniques are widely used to estimate Moho depth, resolving the interface beneath oceanic crust, typically only 5–8 km thick, can be difficult because the Moho phase already arrives 1–2 s after the direct P wave and therefore requires high-frequency data and a strong signal-to-noise ratio (SNR) (Kawakatsu et al., 2009; Audet, 2016). Furthermore, reverberations generated within sedimentary layers and the water column can mask the Moho arrival and reduce vertical resolution, complicating direct interpretation of the interface (Audet, 2016). The autocorrelation approach overcomes several of these challenges by enhancing reflection phases from sharp discontinuities and improving sensitivity to fine-scale lithospheric structure (Sun and Kennett, 2016; Wang et al., 2020). This method has been successfully applied in a range of tectonic environments. For example, Phạm and Tkalčić (2018) and Saneesh et al. (2026) used this technique to estimate ice thickness in Antarctica. Viens et al. (2022) employed P-wave autocorrelation to image the sediment–bedrock interface in the Kanto Basin, Japan. Alemayehu et al. (2023) and Ouammou et al. (2025) delineated Moho structure beneath Ethiopia and Morocco, respectively, while Plescia et al. (2020) in the Bighorn Mountains (Wyoming, USA) and Gupta et al. (2025) in the Himalaya demonstrated the effectiveness of the method for crustal imaging in orogenic settings. Building on these advances, this study aims to derive the crustal structure beneath a geodynamically important sector of the western Indian Ocean, encompassing six volcanic islands—Europa, Grande Glorieuse, Juan de Nova, Mayotte, Tromelin, and La Réunion—to improve our understanding of regional lithospheric processes using teleseismic P-wave coda autocorrelation.

2 Data and Methodology

2.1 Data

In this study, we utilize earthquake data recordings from 61 broadband seismic stations (Supplementary Table S1), comprising 54 ocean-bottom seismometers (OBSs) and 6 land-based stations, deployed during the RHUM-RUM experiments (Barruol et al., 2017), together with a permanent GEOSCOPE station on La Réunion Island (Fig. 1; RER). The RHUM-RUM network spanned an area of roughly 2000 × 2000 km^2. It included 57 broadband OBS stations surrounding La Réunion, complemented by 37 temporary land stations installed on adjacent islands and along the coast of Madagascar. Three OBS stations with operational periods shorter than 5 days were excluded from the analysis. As this study primarily focuses on crustal structure derived from teleseismic P-wave coda autocorrelation of the OBS dataset, only six well-studied land stations, together with the well-established RER station, were retained to provide limited comparison with and validation of the OBS-based results, while also improving spatial coverage.

The RHUM-RUM stations were operated over different time periods between 2011 and 2016, whereas station RER has been in operation since 1986; the corresponding data durations used for each station are listed in Supplementary Table S1. The marine seismic array consisted of broadband OBSs provided by multiple international instrument pools (DEPAS, GEOMAR, and INSU). The instruments were equipped with three-component Güralp CMG-40T sensors with a 60-s corner period and Nanometrics Trillium 240 sensors with a 240-s corner period. Detailed information on instrument specifications and deployment performance is provided in Stähler et al. (2016).

We retrieved vertical-component waveforms of earthquakes with moment magnitude Mw $\geq$ 5.5 and epicentral distances between 30° and 90° from the RESIF data center (Fig. 2) using the ObsPyDMT Python package

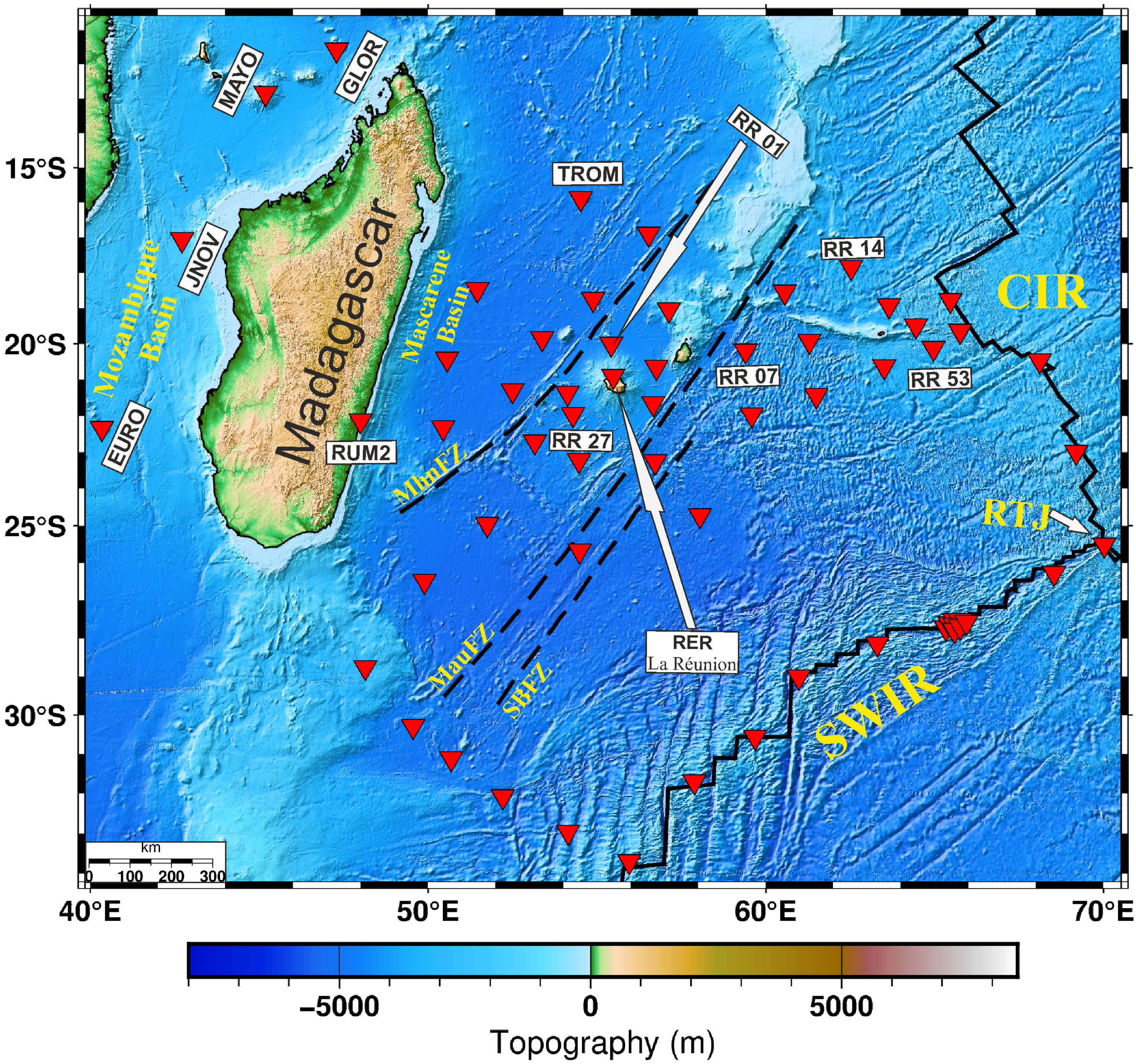

Figure 1 Map of the western Indian Ocean illustrating bathymetry, topography, and the distribution of seismometers. Red triangles mark the positions of the 61 stations analyzed in this work. SWIR: Southwest Indian Ridge; RTJ: Rodrigues Triple Junction; CIR: Central Indian Ridge; MauFZ: Mauritius Fracture Zone; MhnFZ: Mahanoro Fracture Zone; SBFZ: Southern Bous-sole Fracture Zone. Island stations are located on Europa (EURO), Grande Glorieuse (GLOR), Juan de Nova (JNOV), Mayotte (MAYO), Tromelin (TROM), and La Réunion (RER).

(Hosseini and Sigloch, 2017). The epicentral distance range ensures that the direct P-wave arrivals remain well separated from other seismic phases. Each waveform was trimmed to an 80-second window, starting 20 seconds before the theoretical P-wave arrival time predicted by the ak135 velocity model (Kennett et al., 1995). Traces with poor SNR or indistinct P-onset were manually identified and removed from the analysis. The retained traces were resampled at 40 Hz, and both mean and linear trends were removed before further analysis.

2.2 Methodology

Teleseismic waves arriving at a seismic station can be approximated as plane waves (Fig. 3). The P-wave coda of these distant earthquakes contains multiple crustal reverberations that encode information about subsurface interfaces. Autocorrelating the coda waveforms produces a single pulse and its mirrored reflection at time zero, effectively converting the transmission response of the medium into a reflection response (Wapenaar et al., 2004). In this study, we isolate the causal part (positive side) of the signal and suppress the zero-lag pulse using a taper function. The most prominent pulse in the resulting one-sided autocorrelogram, referred to as the $2p$ phase (Fig. 3), corresponds to the P-wave with a single reflection at an interface. This phase represents the cumulative contribution of all signals sharing the same time delay relative to the direct

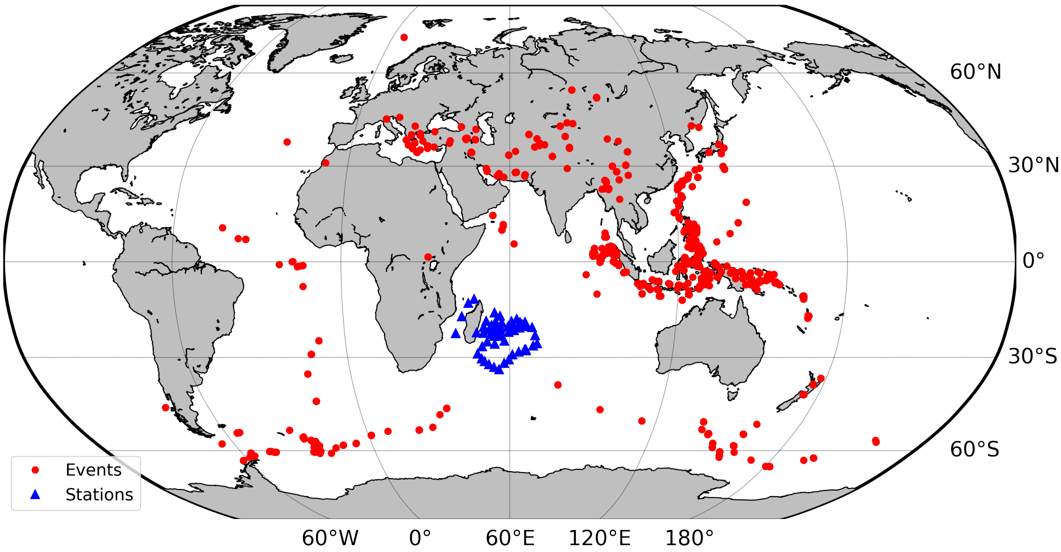

Figure 2 Distribution of teleseismic earthquakes (red dots) and seismic stations (blue triangles) used in this study.

phase ($1p$) and reflected phase ($3p$) (Phạm and Tkalčić, 2018; Phạm, 2019).

The time delay of the $2p$ phase is expressed as:

$$t_{2p} = t_{3p} - t_{1p} = 2H\sqrt{\frac{1}{V_p^2} - \beta^2} \quad (1)$$

where H denotes the depth of the reflector, V_p is the P-wave velocity, and β is the ray parameter. The $2p$ phase typically shows a negative polarity due to the phase reversal caused by free-surface reflection. To enhance these reflection signatures, we adopted the processing strategy of Phạm and Tkalčić (2017) and Phạm (2019).

The pre-processed seismic traces are transformed into the frequency domain using a Fast Fourier Transform (FFT). Their complex spectra are then normalized with an adaptive spectral whitening function, applying a whitening bandwidth (ΔW) determined empirically. This parameter is critical for effectively recovering reflection phases from autocorrelograms, as it governs the extent of spectral smoothing and thus balances noise suppression with the retention of coherent structural information, and helps reduce sediment-related resonance in the autocorrelograms (Wang et al., 2020). Following the approach of Phạm and Tkalčić (2018) and Phạm (2019), ΔW is selected by examining resonance patterns observed in the linear stack of whitened power spectra, which originate from P-wave reverberations within the crust. Supplementary Fig. S1 illustrates the influence of ΔW on vertical-component autocorrelograms at station RR07. Resonance peaks become distinct when ΔW exceeds 0.4 Hz, showing a characteristic spacing of approximately 0.45 Hz, corresponding to a vertical two-way travel time of ~2.2 s, which implies a reflector depth of ~7.3 km, assuming $V_p = 6.65$ km/s. Empirically, the optimal ΔW range corresponds to one to two times the resonance spacing (~0.45 – 0.9 Hz). Additionally, ΔW was found to vary inversely with the depth of the reflecting interface; hence, different stations require slightly different empirically derived ΔW values (Supplementary Table S2). The whitened spectra are autocorrelated and subsequently converted back into the time domain using the Inverse FFT. A cosine taper function is applied to attenuate the central peak of the autocorrelograms, and a zero-phase band-pass filter (0.5–2 Hz) is used to enhance the sharpness of reflection phases. To further improve the SNR and suppress incoherent energy, including source-side scattering, depth phases, and effects related to source time functions, individual autocorrelograms are combined using the phase-weighted stacking (PWS) method of Schimmel and Paulssen (1997) with a stacking order of one (Phạm and Tkalčić, 2017). The resulting PWS stacks reveal distinct negative-polarity phases, interpreted as potential reflections from the Moho discontinuity.

The two-way travel times t_{2p} of the identified reflections are converted to depth using the relation:

$$H \approx \frac{t_{2p}V_p}{2} \quad (2)$$

Constant P-wave velocities of 6.65 km/s for the OBS stations and 6.5 km/s for the land stations, together with a velocity uncertainty (δVp) of 180 m/s, are adopted following Szwillus et al. (2019). The total uncertainty in estimated thickness (δH) is calculated as:

$$\delta H \approx \frac{V_p\,\delta t_{2p} + \delta V_p\,t_{2p}}{2} \quad (3)$$

Here δt_{2p} denotes the uncertainty in the picked delay time of the $2p$ phase. To quantify this, we apply a bootstrap resampling approach (Tibshirani and Efron, 1993), in which individual autocorrelograms for each station component are resampled with replacement, and the reflection delay times were selected from each

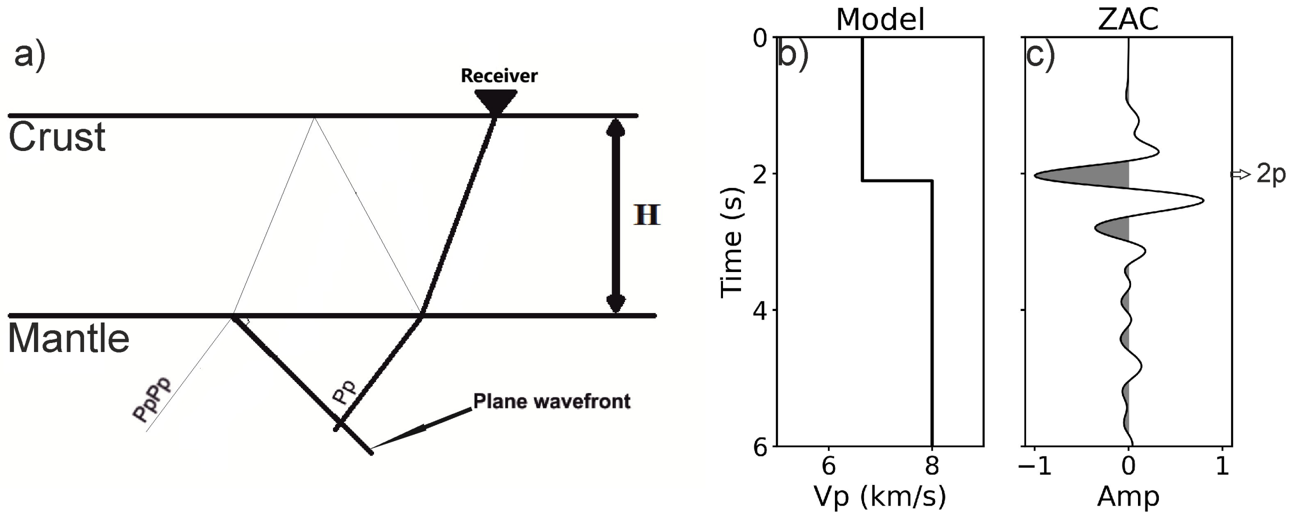

Figure 3 (a) Schematic illustration of P-wave reverberations within a layer of thickness H overlying a half-space. (b) A corresponding one-dimensional P-wave velocity model, assuming a constant P-wave velocity of 6.65 km/s within the layer, was used as input for the analysis. (c) One-sided vertical-component autocorrelogram (ZAC) derived from the model, where $2p$ denotes the P-wave single reflection phase.

resampled stack. The standard deviation derived from 100 bootstrap iterations is taken as the uncertainty in the time delay.

2.3 Synthetic Experiment

Before applying the technique to real data, we conducted a synthetic experiment to evaluate the effectiveness of the P-wave coda autocorrelation technique in resolving a major subsurface discontinuity in the oceanic environment. The experiment simulates full seismograms recorded by a receiver on the abyssal plain above a horizontally layered medium, with a water column overlain. The interface is modeled to represent the Moho and exhibits a positive reflection coefficient. Because the events considered are teleseismic, with epicentral distances >2500 km, which is much greater than the depth range of interest, the incoming waves can be approximated as plane waves.

First, we generate the structural impulse response to a plane-wave arrival at an OBS located on the abyssal plain at 4000 m below sea level using the open-source Python package Telewavesim (Audet et al., 2019). The model includes an overlying water column with a velocity of 1500 m/s and a density of 1027 kg/m^3 (Raitt, 1963). A one-dimensional Earth model with a 7 km-thick crust and an average P-wave velocity of 6.65 km/s was used (Fig. 4a; Szwillus et al., 2019). Epicentral distances are converted to ray parameters to define the incidence angle of the incoming plane wave. Second, we simulate the source-time function and propagation effects by creating randomized low-frequency waveforms. For that, we generate an array of normally distributed random numbers with a mean of zero and a standard deviation of one, with a time duration uniformly distributed between 8 and 12 s, approximately equivalent to a Mw 6.0 earthquake. This time series is low-pass filtered using a third-order Butterworth filter to emphasize the low-frequency content and tapered at both ends. The corner frequency is randomly selected between 0 and 0.5 Hz. The final synthetic seismograms are obtained by convolving the structural impulse response with the random source waveforms for each epicentral distance. An example of the waveform component and the complete synthetic seismogram is shown in Fig. S2 of the supplementary material. The synthetic traces are then autocorrelated using a spectral whitening bandwidth of 0.5 Hz and a zero-phase band-pass filter between 0.5 and 2 Hz (Fig. 4b), and subsequently stacked using phase-weighted stacking (PWS; Fig. 4c).

The resulting PWS clearly reveals a pronounced negative-polarity arrival at the expected travel time (~2.1 s) of the reflected P-wave (2p), demonstrating the method's reliability and resolving power. The PWS also shows the effect of water-column reverberation, marked as WCR. The arrival times (t_w) of these pressure reverberations accumulate with delays proportional to the water-column thickness, occurring at integer multiples of

$$t_w = h_w \sqrt{\frac{1}{c^2} - q^2} \tag{4}$$

where h_w is the water depth, c is the acoustic velocity and q is the horizontal slowness. In our case, however, these reverberations do not significantly affect crustal thickness estimation, because all OBS stations used in this study are located at sufficiently large water depths (Supplementary Table S1), causing water-column multiples to arrive relatively late in the P-wave coda and therefore not interfere with the Moho-related phase (Fig. 4; Fig. S2). Moreover, we do not observe significant water multiples in either the teleseismic waveforms or the corresponding autocorrelograms (Fig. S3). The weak expression of WCR may reflect seafloor properties, including low impedance contrasts at the water–seafloor interface, which can reduce the strength of water-column multiples in OBS data (Thorwart and Dahm, 2005). We therefore infer that WCR exerts only a

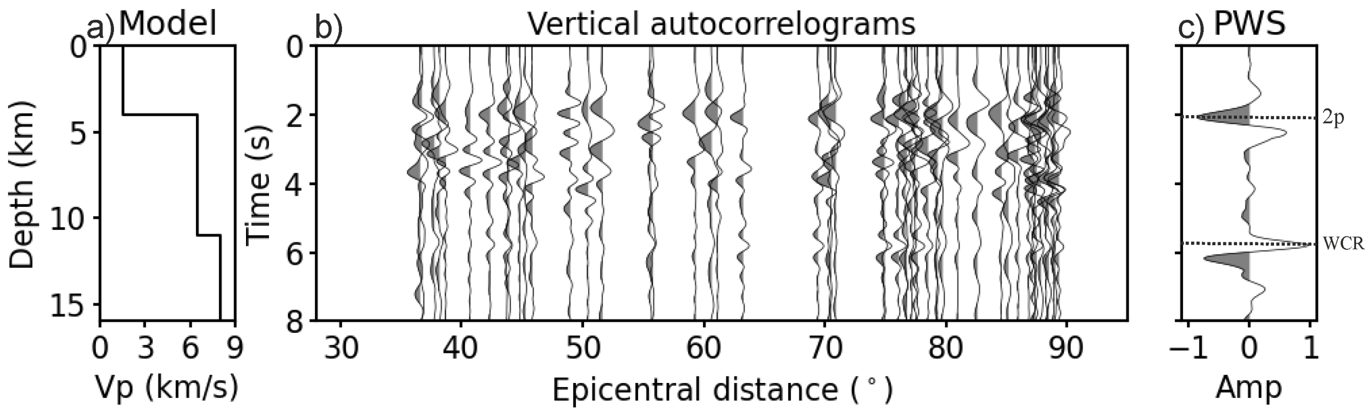

Figure 4 (a) Input one-dimensional P-wave velocity model consisting of a 4 km-thick water layer with $V_p = 1.5$ km/s, overlying an oceanic crustal layer with $V_p = 6.65$ km/s and a major discontinuity, interpreted as the Moho, at 7 km below the seafloor. (b) One-sided vertical autocorrelograms of individual synthetic events are displayed as a function of epicentral distance. (c) PWS of the one-sided vertical autocorrelograms, where $2p$ denotes the phase associated with reflections from the Moho, and the water column reverberation phase (WCR) is also indicated.

negligible influence on the crustal thickness estimates derived in this study.

3 Results

We estimated the crustal thickness beneath 61 broadband seismic stations (7 land stations and 54 OBSs) distributed across the study area (Supplementary Table S2). The $2p$ delay time was determined from the prominent negative phase identified in the stacked vertical autocorrelograms. Fig. 5 presents examples of individual event autocorrelograms and their PWS for four stations, including one land station on La Réunion (RER) and three OBS positioned throughout the study region (RR01, RR07, RR27). The locations of these stations are shown in Fig. 1. In each example, the dominant negative phase ($2p$ reflection phase) in individual autocorrelograms is marked with a black dashed line. The examples illustrate that individual autocorrelograms can become noisy, making the identification of major reflection phases challenging. To address this, we applied PWS, which strengthens coherent reflection phases while suppressing random noise. The PWS autocorrelograms for the remaining stations are presented in Supplementary Figures S3-S6. Station RER (Fig. 5a) exhibits a dominant negative phase at ∼4.5 ± 0.018 s, corresponding to a comparatively thick crust of ∼14.63 ± 0.47 km. Although the phase coherence in individual autocorrelograms at RER is weaker than that observed for the OBS stations, the stacked result reveals a clearer and more stable Moho-related phase. This emphasizes the importance of stacking, which enhances persistent Moho signals while suppressing incoherent noise and event-dependent variability. The reduced coherence of individual autocorrelograms at RER may reflect both data quality and structural factors. In addition to elevated ambient noise levels typical of island stations (Stutzmann et al., 2000), previous studies suggest the presence of magmatic underplating beneath La Réunion (Fontaine et al., 2015), resulting in a more gradational crust–mantle transition rather than a sharp interface (Dofal, 2021). This reduces the impedance contrast at the Moho and may lead to weaker and less coherent reflected phases in individual traces. In contrast, station RR01 (Fig. 5b) shows its principal negative phase at ∼2.15 ± 0.020 s, indicating a crustal thickness of ∼7.15 ± 0.26 km. Similarly, RR07 (Fig. 5c) displays a negative phase at ∼2.23 ± 0.018 s, corresponding to a thickness of ∼7.40 ± 0.26 km, whereas RR27 (Fig. 5d) yields a delay time of ∼2.30 ± 0.017 s and an inferred crustal thickness of ∼7.65 ± 0.26 km.

We linearly interpolate the crustal thickness estimates from all 61 stations to generate a spatial map of crustal structure and the associated uncertainty distribution (Fig. 6). The corresponding distribution of $2p$ delay times is shown in Supplementary Fig. S7. The Madagascar region is masked in our crustal thickness map (Fig. 6) because Madagascar itself is underlain by continental crust, where significant lateral variations in crustal thickness are expected and cannot be reliably constrained with the available data. In contrast, the area near the SWIR, although it also has relatively sparse station coverage, is not masked. This region lies within the oceanic crust, where crustal thickness variations are typically more gradual and fall within a narrower range, allowing meaningful interpolation even with fewer observations. Across the entire study region, $2p$ delay times range from approximately 1.3 to 7.9 s, implying crustal thickness variations of ∼4.3 to ∼25.8 km. The associated uncertainties range from ∼0.014 to 0.181 s, translating to thickness uncertainties of ∼0.18 to 0.79 km.

The thickest crust is observed beneath station RUM2 (∼25.8 ± 0.77 km) on the eastern coast of Madagascar, whereas the thinnest crust occurs beneath OBS station RR53 (∼4.3 ± 0.19 km). The OBS stations show a mean delay time of ∼2.10 ± 0.022 s, yielding an average crustal thickness of ∼7.01 ± 0.27 km. As expected, the land stations exhibit a higher average $2p$ delay time of ∼5.48 ± 0.018 s, corresponding to a crustal thickness of ∼17.82 ± 0.53 km. Among the land stations, EURO on Europa Island shows a prominent negative phase at ∼5.10 ± 0.02 s,

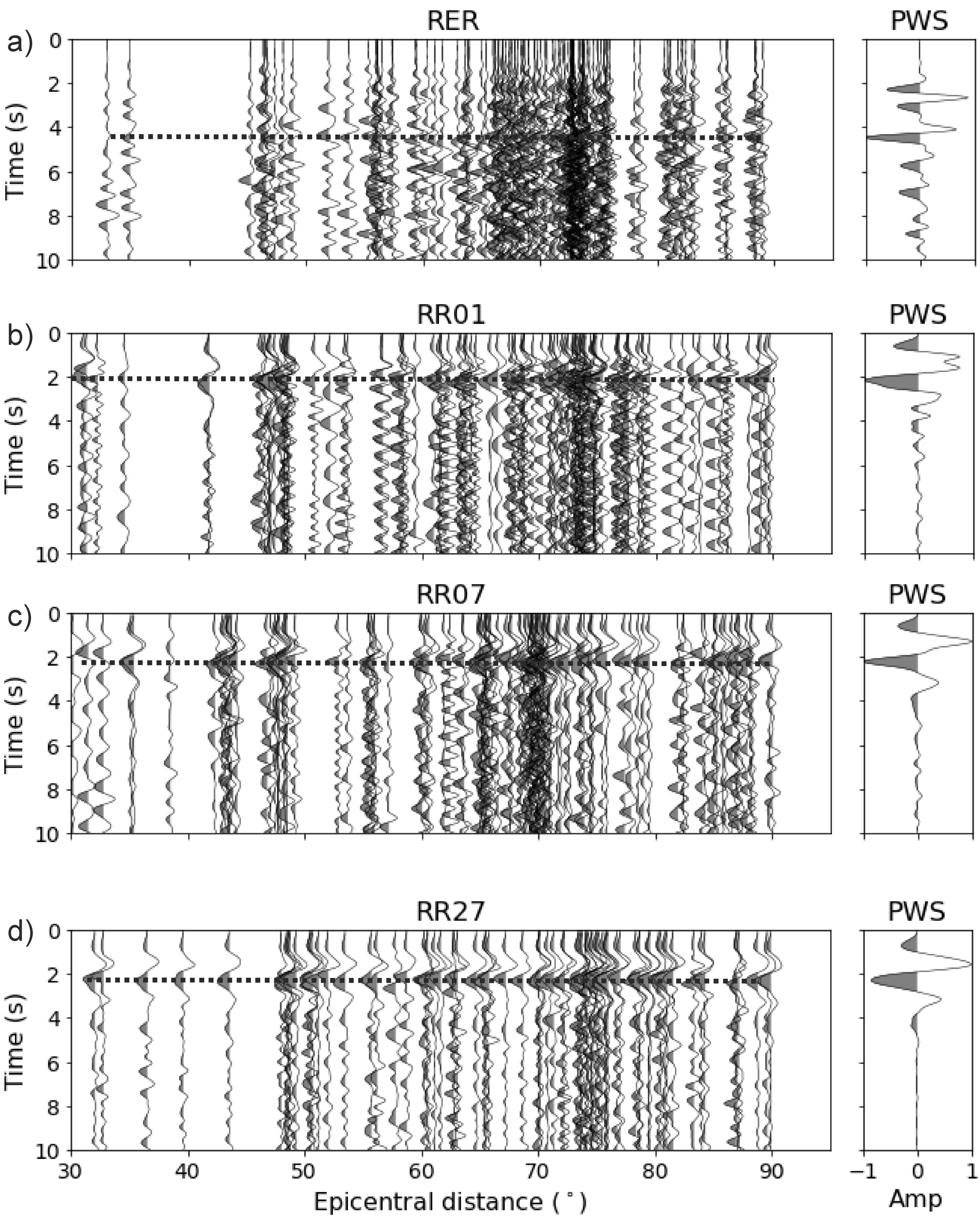

Figure 5 Individual vertical autocorrelograms as a function of epicentral distance (°) (left) and their corresponding PWS vertical autocorrelograms (right) for four representative stations (RER, RR01, RR07, and RR27) shown in Fig. 1. The dashed lines highlight the coherent phase across the autocorrelograms, interpreted as the Moho discontinuity. The PWS autocorrelograms for the remaining stations are presented in Supplementary Fig. S3-S6.

corresponding to an average crustal thickness of ∼16.58 ± 0.52 km. At GLOR on Grande Glorieuse Island, the phase occurs at ∼3.45 ± 0.01 s, indicating a thickness of ∼11.21 ± 0.37 km. Station JNOV on Juan de Nova Island exhibits a delay of ∼5.72 ± 0.01 s, resulting in a crustal thickness of ∼18.61± 0.57 km. At MAYO on Mayotte Island, the main negative phase at ∼7.38 ± 0.02 s corresponds to a thickness of ∼23.98 ± 0.72 km. Whereas station TROM on Tromelin Island exhibits a delay of ∼3.30 ± 0.02 s, consistent with a crustal thickness of ∼10.73 ± 0.37 km.

4 Discussion

In this study, crustal thickness refers to the depth from the station level to the Moho discontinuity (i.e., below station level, bst) identified from the autocorrelation analysis. For volcanic island stations (RER, TROM, GLOR, EURO, JNOV, and MAYO), this definition includes both the underlying pre-existing crust and the overlying volcanic edifice. To compare stations at different elevations, we shifted the single-station models so that all reported depths are referenced to sea level (bsl); these values are listed in Supplementary Table S2. Previous receiver function studies in the region have also provided important constraints on crustal thickness (e.g., Fontaine et al., 2015; Dofal, 2021; Dofal et al., 2023). Building on these earlier results, the autocorrelation method applied here offers greater sensitivity to fine-scale lithospheric structure and reduces sediment-related resonance in autocorrelograms through spectral whitening (Wang et al., 2020), thereby enabling clearer and more robust imaging of the oceanic Moho. However, independent constraints on sediment thickness beneath the stations could further refine the velocity model used for time-to-depth conversion and improve the resulting crustal thickness estimates.

4.1 Crustal Thickness Beneath Volcanic Islands and Continental Margin

We estimate crustal thickness beneath six volcanic islands, as well as one station located along the eastern coast of Madagascar. The islands of Europa, Grande Glorieuse, Juan de Nova, and Mayotte are situated within the Mozambique Channel, where the nature of the underlying lithosphere remains a subject of active debate. Moreover, the recent seismic crisis near Mayotte (Dofal et al., 2021; Cesca et al., 2020), the plume-related volcanism at La Réunion (Li et al., 2003), and the tectonomagmatic complexity of the Mascarene Basin near Tromelin highlight the importance of obtaining robust crustal thickness constraints to better understand the tectonic and magmatic evolution of the western Indian Ocean. The RUM2 station yields a crustal thickness of ∼25.85 ± 0.77 km, consistent with values expected for continental crust within the Androy volcanic domain, which was intruded by the Ambalavao magmatic suite between ∼550 and 510 Ma (Tucker et al., 2014). This estimate is in good agreement with the findings of Rindraharisaona et al. (2017), who reported a Moho depth of 29 ± 1.5 km at the same site using joint inversion of RFs and surface-wave dispersion data. Considering the uncertainties associated with these different techniques, the two estimates fall within overlapping error ranges, reinforcing the robustness of the crustal thickness obtained in this study.

Europa Island is situated on oceanic crust that lies at a depth of approximately 3 km below sea level (Smith and Sandwell, 1997). Our analysis indicates a corresponding Moho depth of approximately 16.58 ± 0.52 km (bst). The presence of such a relatively thick crust beneath Europa is consistent with previous observations by Mueller and Jokat (2017) and Dofal et al. (2021). This thickening could be caused by magmatic underplating associated with prolonged and polyphase volcanic activity in the region, as suggested by the island's tectonomagmatic setting and the magmatic events documented in the surrounding area (Georgen et al., 2001; Courgeon et al., 2016). Grande Glorieuse Island shows a Moho depth of 11.21 ± 0.37 km (bst), in close agreement with the receiver function estimate of 11.6 ± 0.02 km reported by Dofal et al. (2021), as well as with the independent observations of Phethean et al. (2016). Juan de Nova Island, located on a ∼2 km-deep seafloor (Smith and Sandwell, 1997), displays a comparatively thick crust of ∼18.61 ± 0.57 km (bst). This value is consistent with the ∼20 km Moho depth reported by Vormann et al. (2020) and Dofal et al. (2021), and likely reflects crustal thinning from an originally ∼35 km–thick continental crust during the opening of the Mozambique Channel (Andriampenomanana et al., 2017). Mayotte Island shows an even greater Moho depth of ∼23.98± 0.72 km (bst), which agrees well with the H–κ stacking result of ∼25.86 ± 3.9 km reported by Dofal et al. (2021). This substantial crustal thickness may be attributed to long-lived magmatic underplating associated with approximately 20 Myr of volcanic activity (Michon, 2015).

The crustal thickness estimated at the RER station on La Réunion (∼14.63 ± 0.47 km) is in close agreement with previous RF studies conducted at the same station. Earlier analyses of RER based on RF inversion and joint inversion approaches generally report Moho depths of ∼13–14 km (Fontaine et al., 2015; Dofal, 2021), along with a shallow low-velocity zone at ∼2–3 km depth, interpreted as the volcanic edifice (Zelt and Ellis, 1999; Fontaine et al., 2015). Independent constraints from seismic refraction profiles further support a Moho depth of ∼13 km (Charvis et al., 1999; Gallart et al., 1999; Gupta et al., 2010). The close correspondence between our estimate and those derived from independent analyses supports the robustness of the inferred Moho depth beneath La Réunion. The moderately thick crust beneath the island is likely associated with magmatic underplating linked to hotspot-related volcanic activity; however, the presence of efficient magma ascent pathways and limited underplating may have constrained excessive crustal thickening, as suggested by previous studies (Hable et al., 2019). The crustal thickness beneath Tromelin Island is estimated to be ∼10.73 ± 0.37 km, a value that aligns well with previous receiver function results of ∼9 km reported by Barruol et al. (2018) and Dofal (2021). This agreement suggests that the Mascarene Basin, where Tromelin is located, is underlain by comparatively thin oceanic crust, in contrast to the thicker crust observed in the nearby Mozambique Channel.

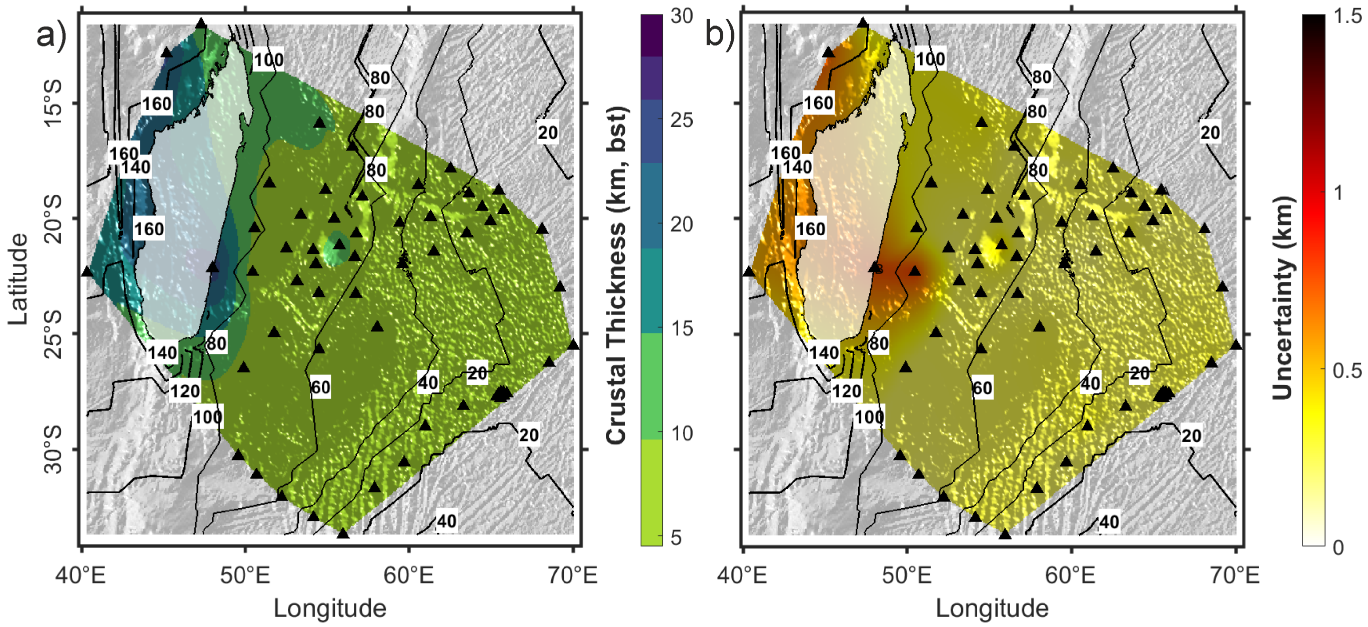

Figure 6 (a) Crustal thickness map (linearly interpolated) shown relative to station level (bst) and (b) the corresponding uncertainty distribution across the study area. Black triangles indicate seismic station locations. Black solid lines denote seafloor age contours, with ages labeled in white boxes near the contours in Ma. The region over Madagascar is masked.

4.2 Crustal thickness variation across the oceanic domain

As illustrated in Fig. 6a, crustal thickness across the oceanic domain varies from ∼4.3 ± 0.18 km to ∼8.89 ± 0.31 km. The mean oceanic crustal thickness derived in this study (∼7.01 ± 0.27 km) is consistent with the global average reported in CRUST1.0 (Laske et al., 2013). The oceanic lithosphere beneath the study region spans an age range of 0–160 Ma (Fig. 6), with younger crust occurring near spreading ridges such as the SWIR and CIR, and progressively older crust characterizing the major seafloor basins, including the Mascarene Basin (∼90 Ma) and the Mozambique Channel (∼150 Ma). Although an apparent spatial correlation between crustal thickness and plate age can be observed in our dataset, this relationship should not be interpreted as evidence for progressive crustal thickening through time. Instead, crustal thickness largely reflects the magmatic and tectonic conditions prevailing at the time of formation (e.g., Wang et al., 2011). An overall oceanic crustal thickness of ∼5–6 km is observed around the SWIR and CIR, consistent with the normal oceanic crust formed at spreading centers (Wang et al., 2011). Localized undulations are present, which may reflect variations in magmatic activity, including episodic or focused melt delivery from the upper mantle that can locally thicken the crust (e.g., Li et al., 2015). Farther from the ridges, the Mascarene Basin exhibits an average crustal thickness of ∼10 km, whereas the Mozambique islands are underlain by thicker crust, averaging ∼17 km. These thicker crusts likely reflect a combination of magmatic addition, including hotspot-related volcanism and magmatic underplating, and the inheritance of stretched and thinned continental crust associated with the opening of the Mozambique Channel (Charvis et al., 1999; Fontaine et al., 2015; Andriampenomanana et al., 2017; Dofal et al., 2021; Dofal, 2021).

To examine lateral variations in crustal thickness in greater detail, we constructed four profiles across the study region and projected stations located within 50 km of each profile onto the corresponding sections (Fig. 7). Along profiles A–B and G–H (Fig. 7a and 7d), the Moho is relatively flat, with depths ranging from ∼10.3 to 11.6 km and ∼8.8 to 11.8 km (bsl), respectively, indicating laterally uniform oceanic crust in these areas. By contrast, profiles crossing La Réunion (Fig. 7b and 7c) show a localized Moho deepening to ∼13.8 km (bsl), highlighting a distinct crustal root beneath the island relative to the surrounding basin. This geometry is consistent with previous studies that infer a magmatically modified crust beneath La Réunion, including an underplated body at the base of the crust and an overlying volcanic edifice (Charvis et al., 1999; Gallart et al., 1999; Fontaine et al., 2015; Dofal, 2021).

5 Conclusion

This study provides a detailed characterization of crustal thickness beneath the western Indian Ocean using the teleseismic P-wave coda autocorrelation method applied to the earthquake data from 54 OBSs and 7 land seismic stations. The resulting crustal thickness estimates reveal significant spatial variability, ranging from ∼4.3 km beneath the oceanic crust near CIR to ∼25.85 km beneath the eastern coast of Madagascar. The mean oceanic crustal thickness of ∼7 km is consistent with global averages, whereas locally thickened regions beneath volcanic islands such as Mayotte, La Réunion, and Europa suggest magmatic underplating and hotspot-related crustal accretion. The distinct deepening of the Moho beneath La Réunion supports the presence of a magmatic underplated layer linked to the is-

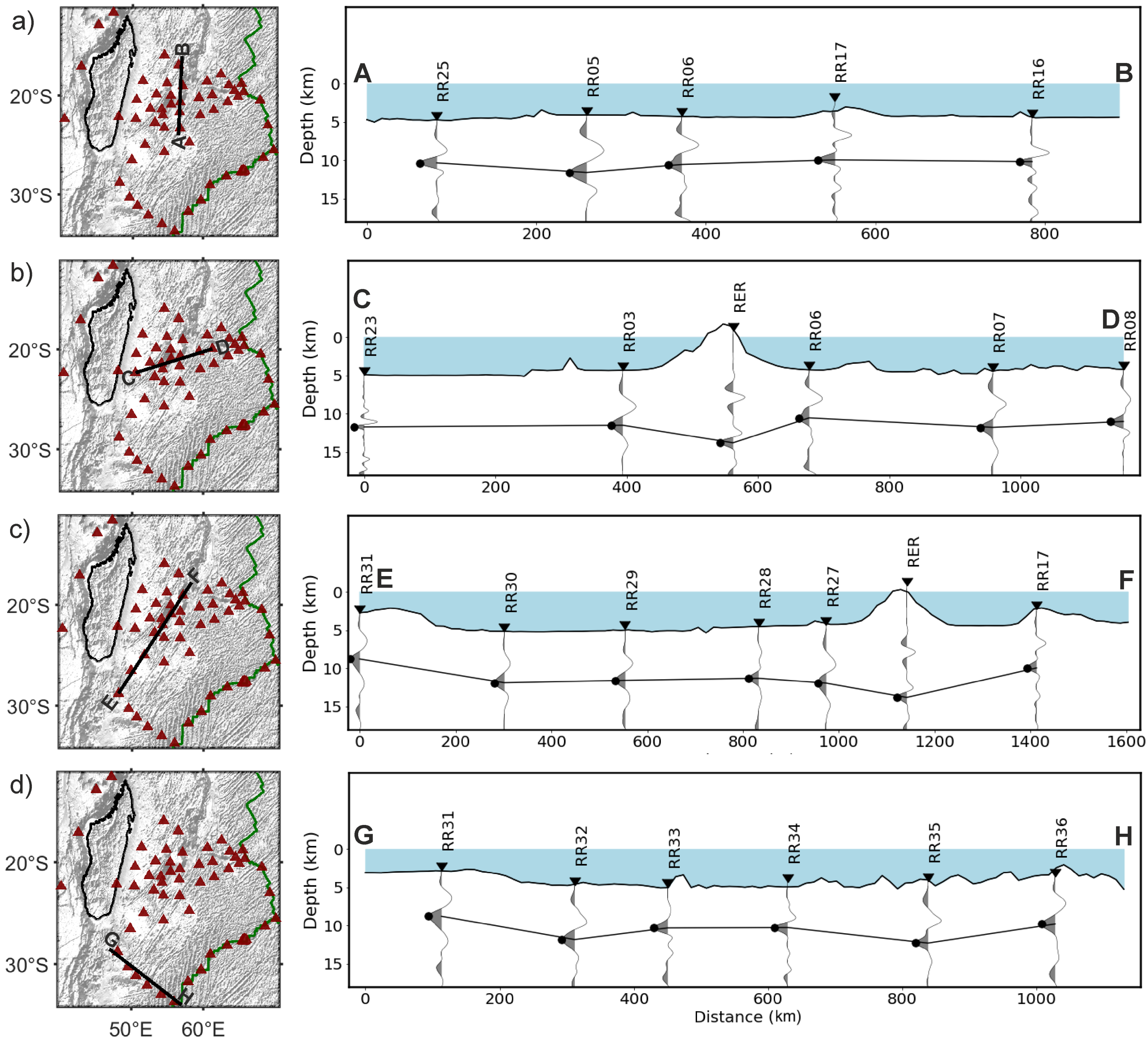

Figure 7 (a–d) Maps of the study area showing the locations of four profiles (left panels) and the corresponding PWS vertical waveforms from stations within 50 km of each profile (right panels), highlighting variations in crustal thickness along the profiles. In the left panels, black straight lines indicate profile locations, red triangles mark seismic stations, and green lines denote spreading ridges. The geographical boundary of Madagascar is also shown. In the right panels, black triangles mark the projected positions of seismic stations, with station names labelled above. Black dots denote the prominent negative phases in each autocorrelogram, and the connecting black line traces the inferred crustal thickness variation along each profile.

land's hotspot activity. These findings offer new quantitative constraints on crustal architecture and provide a valuable foundation for future investigations into the tectono-magmatic processes that govern crustal formation, modification, and isostatic compensation in this geodynamically complex region.

Acknowledgements

We gratefully acknowledge the International Federation of Digital Seismograph Networks (FDSN), the Incorporated Research Institutions for Seismology (IRIS), the GEOSCOPE network, and the RESIF Data Center for providing access to high-quality seismic data from both OBSs and land-based stations. We thank Dr. T. S. Phạm for kindly sharing his Ph.D. thesis with us. We are grateful to the editor, Dr. Anant Hariharan, and to both reviewers, Dr. T. S. Phạm and Dr. Guilhem Barruol, for their critical and constructive comments, which helped improve the original manuscript. TSS acknowledges the support of the University Grants Commission through a Senior Research Fellowship, which supported his Ph.D. research. TSS and SG acknowledge the support of the CSIR-NGRI for this study. DS acknowledges the support by FCT, I.P./MCTES through national funds

(PIDDAC): LA/P/0068/2020 (https://doi.org/10.54499/LA/P/0068/2020), UID/50019/2025 (https://doi.org/10.54499/UID/50019/2025), UID/PRR/50019/2025 (https://doi.org/10.54499/UID/PRR/50019/2025), UID/PRR2/50019/2025 (https://doi.org/10.54499/UID/PRR2/50019/2025).
CSIR–NGRI reference number for this manuscript is NGRI/Lib/2026/Pub-73.

Data and code availability

The RHUM-RUM seismic data are freely available through the RESIF Data Centre (http://seismology.resif.fr), where they are archived under the FDSN network code YV. Data from the RER station are also available via the RESIF Data Centre under FDSN network code G (http://ws.resif.fr/fdsnws/dataselect/1/). The code used to compute the whitened autocorrelation in this study is publicly available on GitHub (https://github.com/tsonpham/PCodaAutocorrelation). The plots presented in this work were generated using PyGMT (Wessel et al., 2019) and MATLAB.

Ethical Statement

This research did not require ethics committee approval.

Competing interests

The authors declare that they have no competing interests.

References

Alemayehu, S., Aoudia, A., Ayele, A., Pachhai, S., Ebinger, C. J., Thapa, H. R., Kherchouche, R., Guidarelli, M., and Kim, S. Structure of the Crust-Uppermost Mantle Beneath the Ethiopian Volcanic Province Using Ambient Seismic Noise and Teleseismic P Wave Coda Autocorrelation. *Tectonophysics*, 869:230092, 2023. doi: 10.2139/ssrn.4314889.

Andriampenomanana, F., Nyblade, A. A., Wysession, M. E., Durrheim, R. J., Tilmann, F., Julià, J., Pratt, M. J., Rambolamanana, G., Alexqabi, G., Shore, P. J., and Rakotondraibe, T. The structure of the crust and uppermost mantle beneath Madagascar. *Geophysical Journal International*, 210(3), 2017. doi: 10.1093/gji/ggx243.

Audet, P. Receiver functions using OBS data: promises and limitations from numerical modelling and examples from the Cascadia Initiative. *Geophysical Journal International*, 205(3): 1740–1755, Mar. 2016. doi: 10.1093/gji/ggw111.

Audet, P., Thomson, C., Bostock, M., and Eulenfeld, T. Telewavesim: Python software for teleseismic body wave modeling. *Journal of Open Source Software*, 4(44):1818, Dec. 2019. doi: 10.21105/joss.01818.

Barruol, G. and Sigloch, K. Investigating La Réunion hot spot from crust to core. *Eos, Transactions American Geophysical Union*, 94 (23), 2013. doi: 10.1002/2013eo230002.

Barruol, G., Sigloch, K., Group, R.-R., and RESIF. RHUM-RUM experiment, 2011-2015, code YV (Réunion Hotspot and Upper Mantle – Réunion's Unterer Mantel) funded by ANR, DFG, CNRS-INSU, IPEV, TAAF, instrumented by DEPAS, INSU-OBS, AWI and the Universities of Muenster, Bonn, La Réunion [Data set]. *RESIF—Réseau Sismologique et géodésique Français*, 2017. doi: 10.15778/RESIF.YV2011.

Barruol, G., Dofal, A., Fontaine, F., Michon, L., and Tkalcic, H. Crustal structure variation across the southwestern Indian Ocean from receiver functions determined at Ocean-Bottom Seismometers. In *AGU Fall Meeting Abstracts*, volume 2018, pages T43G–0497, 2018.

Barruol, G., Sigloch, K., Scholz, J.-R., Mazzullo, A., Stutzmann, E., Montagner, J.-P., Kiselev, S., Fontaine, F. R., Michon, L., Deplus, C., and Dyment, J. Large-scale flow of Indian Ocean asthenosphere driven by Réunion plume. *Nature Geoscience*, 12(12): 1043–1049, Nov. 2019. doi: 10.1038/s41561-019-0479-3.

Cesca, S., Letort, J., Razafindrakoto, H. N. T., Heimann, S., Rivalta, E., Isken, M. P., Nikkhoo, M., Passarelli, L., Petersen, G. M., Cotton, F., and Dahm, T. Drainage of a deep magma reservoir near Mayotte inferred from seismicity and deformation. *Nature Geoscience*, 13(1):87–93, Jan. 2020. doi: 10.1038/s41561-019-0505-5.

Charvis, P., Laesanpura, A., Gallart, J., Hirn, A., Lépine, J., de Voogd, B., Minshull, T. A., Hello, Y., and Pontoise, B. Spatial distribution of hotspot material added to the lithosphere under La Réunion, from wide-angle seismic data. *Journal of Geophysical Research: Solid Earth*, 104(B2):2875–2893, Feb. 1999. doi: 10.1029/98jb02841.

Courgeon, S., Jorry, S., Camoin, G., BouDagher-Fadel, M., Jouet, G., Révillon, S., Bachèlery, P., Pelleter, E., Borgomano, J., Poli, E., and Droxler, A. Growth and demise of Cenozoic isolated carbonate platforms: New insights from the Mozambique Channel seamounts (SW Indian Ocean). *Marine Geology*, 380:90–105, Oct. 2016. doi: 10.1016/j.margeo.2016.07.006.

Dofal, A. *Structure de la lithosphère de l'océan Indien occidental révélée par la méthode des fonctions récepteur*. PhD thesis, Agence Bibliographique de l'Enseignement Supérieur, 2021. doi: 10.70675/fc8b763bz2c7dz473dz8c3fz74b9e8fa989b.

Dofal, A., Fontaine, F., Michon, L., Barruol, G., and Tkalčić, H. Nature of the crust beneath the islands of the Mozambique Channel: Constraints from receiver functions. *Journal of African Earth Sciences*, 184, 2021. doi: 10.1016/j.jafrearsci.2021.104379.

Dofal, A., Michon, L., Fontaine, F. R., Rindraharisaona, E., Barruol, G., and Tkalčić, H. Imaging the lithospheric structure and plumbing system below the Mayotte volcanic zone. *Comptes Rendus. Géoscience*, 354(S2):47–64, Jan. 2023. doi: 10.5802/crgeos.190.

Fisher, R. L., Sclater, J. G., and McKenzie, D. P. Evolution of the Central Indian Ridge, Western Indian Ocean. *Geological Society of America Bulletin*, 82(3):553, 1971. doi: 10.1130/0016-7606(1971)82[553:eotcir]2.0.co;2.

Fontaine, F. R., Barruol, G., Tkalčić, H., Wölbern, I., Rümpker, G., Bodin, T., and Haugmard, M. Crustal and uppermost mantle structure variation beneath La Réunion hotspot track. *Geophysical Journal International*, 203(1):107–126, Aug. 2015. doi: 10.1093/gji/ggv279.

Gallart, J., Driad, L., Charvis, P., Sapin, M., Hirn, A., Diaz, J., de Voogd, B., and Sachpazi, M. Perturbation to the lithosphere along the hotspot track of La Réunion from an offshore-onshore seismic transect. *Journal of Geophysical Research: Solid Earth*, 104(B2):2895–2908, Feb. 1999. doi: 10.1029/98jb02840.

Georgen, J. E., Lin, J., and Dick, H. J. Evidence from gravity anomalies for interactions of the Marion and Bouvet hotspots with the Southwest Indian Ridge: effects of transform offsets. *Earth and Planetary Science Letters*, 187(3-4):283–300, May 2001. doi: 10.1016/s0012-821x(01)00293-x.

Gupta, S., Mishra, S., and Rai, S. S. Magmatic underplating of crust beneath the Laccadive Island, NW Indian Ocean. *Geophysical Journal International*, 183(2), 2010. doi: 10.1111/j.1365-246x.2010.04759.x.

Gupta, S., Saneesh, A. T. S., Kumar, S., and Sivaram, K. Variation in the Main Himalayan Thrust (MHT) within the Central Himalayan Seismic Gap using teleseismic P-wave coda autocorrelation: implications for seismic hazard. *Geophysical Journal International*, 243(1), Aug. 2025. doi: 10.1093/gji/ggaf325.

Hable, S., Sigloch, K., Stutzmann, E., Kiselev, S., and Barruol, G. Tomography of crust and lithosphere in the western Indian Ocean from noise cross-correlations of land and ocean bottom seismometers. *Geophysical Journal International*, 219(2), 2019. doi: 10.1093/gji/ggz333.

Hosseini, K. and Sigloch, K. ObspyDMT: A Python toolbox for retrieving and processing large seismological data sets. *Solid Earth*, 8(5):1047–1070, 2017. doi: 10.5194/se-8-1047-2017.

Kawakatsu, H., Kumar, P., Takei, Y., Shinohara, M., Kanazawa, T., Araki, E., and Suyehiro, K. Seismic Evidence for Sharp Lithosphere-Asthenosphere Boundaries of Oceanic Plates. *Science*, 324(5926):499–502, Apr. 2009. doi: 10.1126/science.1169499.

Kearey, P., Klepeis, K. A., and Vine, F. J. *Global tectonics*. John Wiley & Sons, 2009.

Kennett, B. L. N., Engdahl, E. R., and Buland, R. Constraints on seismic velocities in the Earth from traveltimes. *Geophysical Journal International*, 122(1), 1995. doi: 10.1111/j.1365-246x.1995.tb03540.x.

Laske, G., Masters, G., Ma, Z., and Pasyanos, M. Update on CRUST1. 0—A 1-degree global model of Earth's crust. In *Geophysical research abstracts*, volume 15, page 2658, 2013.

Li, J., Jian, H., Chen, Y. J., Singh, S. C., Ruan, A., Qiu, X., Zhao, M., Wang, X., Niu, X., Ni, J., and Zhang, J. Seismic observation of an extremely magmatic accretion at the ultraslow spreading Southwest Indian Ridge. *Geophysical Research Letters*, 42(8): 2656–2663, Apr. 2015. doi: 10.1002/2014gl062521.

Li, X., Kind, R., and Yuan, X. Seismic study of upper mantle and transition zone beneath hotspots. *Physics of the Earth and Planetary Interiors*, 136(1-2):79–92, Apr. 2003. doi: 10.1016/s0031-9201(03)00021-9.

Lénat, J.-F. *A Brief History of the Observation of the Central Area of Piton de la Fournaise*, page 3–21. Springer Berlin Heidelberg, Oct. 2015. doi: 10.1007/978-3-642-31395-0_1.

Mazzullo, A., Stutzmann, E., Montagner, J., Kiselev, S., Maurya, S., Barruol, G., and Sigloch, K. Anisotropic tomography around La Réunion island from Rayleigh waves. *Journal of Geophysical Research: Solid Earth*, 122(11):9132–9148, Nov. 2017. doi: 10.1002/2017jb014354.

Michon, L. *The Volcanism of the Comoros Archipelago Integrated at a Regional Scale*, page 333–344. Springer Berlin Heidelberg, Oct. 2015. doi: 10.1007/978-3-642-31395-0_21.

Mueller, C. O. and Jokat, W. Geophysical evidence for the crustal variation and distribution of magmatism along the central coast of Mozambique. *Tectonophysics*, 712-713:684–703, Aug. 2017. doi: 10.1016/j.tecto.2017.06.007.

Ouammou, H., Aoudia, A., Javed, F., Thapa, H. R., Tahayt, A., and Wang, H. The Morocco High Atlas 6.8 magnitude 2023 event: New insights from geodetic and seismological modeling. In *EGU General Assembly Conference Abstracts*, pages EGU25–18488. Copernicus GmbH, 2025. doi: 10.5194/egusphere-egu25-18488.

Owen-Smith, T., Ashwal, L., Torsvik, T., Ganerød, M., Nebel, O., Webb, S., and Werner, S. Seychelles alkaline suite records the culmination of Deccan Traps continental flood volcanism. *Lithos*, 182-183:33–47, Dec. 2013. doi: 10.1016/j.lithos.2013.09.011.

Phethean, J. J., Kalnins, L. M., van Hunen, J., Biffi, P. G., Davies, R. J., and McCaffrey, K. J. Madagascar's escape from <scp>A</scp>frica: A high-resolution plate reconstruction for the <scp>W</scp>estern <scp>S</scp>omali <scp>B</scp>asin and implications for supercontinent dispersal. *Geochemistry, Geophysics, Geosystems*, 17(12):5036–5055, Dec. 2016. doi: 10.1002/2016gc006624.

Phạm, T. and Tkalčić, H. On the feasibility and use of teleseismic P wave coda autocorrelation for mapping shallow seismic discontinuities. *Journal of Geophysical Research: Solid Earth*, 122 (5):3776–3791, May 2017. doi: 10.1002/2017jb013975.

Phạm, T. and Tkalčić, H. Antarctic ice properties revealed from teleseismic P wave coda autocorrelation. *Journal of Geophysical Research: Solid Earth*, 123(9), 2018. doi: 10.1029/2018jb016115.

Phạm, T.-S. *Advancing correlation methods of earthquake coda in seismic body wave studies*. PhD thesis, Australian National University, 2019. doi: 10.25911/5de77d634cc16.

Plescia, S. M., Sheehan, A. F., Haines, S. S., Worthington, L. L., Cook, S., and Ball, J. S. Teleseismic P-wave coda autocorrelation imaging of crustal and basin structure, Bighorn Mountains Region, Wyoming, USA. *Bulletin of the Seismological Society of America*, 111(1):466–475, Nov. 2020. doi: 10.1785/0120200177.

Raitt, R. 6. THE CRUSTAL ROCKS. *The Earth Beneath the Sea: History*, 3:85, 1963.

Rindraharisaona, E. J., Tilmann, F. J., Yuan, X., Dreiling, J., Priestley, K. F., Barruol, G., and Wysession, M. E. Lithosphere structure in Madagascar as revealed from receiver functions and surface waves analysis. In *AGU Fall Meeting Abstracts*, volume 2017, pages DI23A–0409, 2017.

Saneesh, A. T., Gupta, S., and Akilan, A. Ice Thickness Estimation Beneath East Antarctica Using Teleseismic P-wave Coda Autocorrelation. *Journal Of The Geological Society Of India*, 102(3): 360–365, Mar. 2026. doi: 10.17491/jgsi/2026/174358.

Schimmel, M. and Paulssen, H. Noise reduction and detection of weak, coherent signals through phase-weighted stacks. *Geophysical Journal International*, 130(2):497–505, Aug. 1997. doi: 10.1111/j.1365-246x.1997.tb05664.x.

Smith, W. H. F. and Sandwell, D. T. Global Sea Floor Topography from Satellite Altimetry and Ship Depth Soundings. *Science*, 277 (5334), 1997. doi: 10.1126/science.277.5334.1956.

Steinhart, J. Mohorovičić discontinuity. *International dictionary of geophysics*, 2:991–994, 1967.

Stutzmann, E., Roult, G., and Astiz, L. GEOSCOPE station noise levels. *Bulletin of the Seismological Society of America*, 90(3): 690–701, 2000. doi: 10.1785/0119990025.

Stähler, S. C., Sigloch, K., Hosseini, K., Crawford, W. C., Barruol, G., Schmidt-Aursch, M. C., Tsekhmistrenko, M., Scholz, J.-R., Mazzullo, A., and Deen, M. Performance report of the RHUM-RUM ocean bottom seismometer network around La Réunion, western Indian Ocean. *Advances in Geosciences*, 41:43–63, Feb. 2016. doi: 10.5194/adgeo-41-43-2016.

Sun, W. and Kennett, B. L. N. Receiver structure from teleseisms: Autocorrelation and cross correlation. *Geophysical Research Letters*, 43(12), 2016. doi: 10.1002/2016gl069564.

Szwillus, W., Afonso, J. C., Ebbing, J., and Mooney, W. D. Global Crustal Thickness and Velocity Structure From Geostatistical Analysis of Seismic Data. *Journal of Geophysical Research: Solid Earth*, 124(2):1626–1652, Feb. 2019. doi: 10.1029/2018jb016593.

Thorwart, M. and Dahm, T. Wavefield decomposition for passive ocean bottom seismological data. *Geophysical Journal International*, 163(2):611–621, Nov. 2005. doi: 10.1111/j.1365-246x.2005.02761.x.

Tibshirani, R. J. and Efron, B. An introduction to the bootstrap. *Monographs on statistics and applied probability*, 57(1):1–436, 1993. doi: 10.1201/9780429246593.

Tsekhmistrenko, M., Sigloch, K., Hosseini, K., and Barruol, G. A tree of Indo-African mantle plumes imaged by seismic tomography. *Nature Geoscience*, 14(8):612–619, 2021. doi: 10.1038/s41561-021-00762-9.

Tucker, R., Roig, J., Moine, B., Delor, C., and Peters, S. A geological synthesis of the Precambrian shield in Madagascar. *Journal of African Earth Sciences*, 94, 2014. doi: 10.1016/j.jafrearsci.2014.02.001.

Viens, L., Jiang, C., and Denolle, M. A. Imaging the Kanto Basin seismic basement with earthquake and noise autocorrelation functions. *Geophysical Journal International*, 230(2):1080–1091, Apr. 2022. doi: 10.1093/gji/ggac101.

Vormann, M., Franke, D., and Jokat, W. The crustal structure of the southern Davie Ridge offshore northern Mozambique–A wide-angle seismic and potential field study. *Tectonophysics*, 778: 228370, Mar. 2020. doi: 10.1016/j.tecto.2020.228370.

Wang, C., Tauzin, B., Pham, T., and Tkalčić, H. On the efficiency of P-Wave coda autocorrelation in recovering crustal structure: examples from dense arrays in the Eastern United States. *Journal of Geophysical Research: Solid Earth*, 125(12), Nov. 2020. doi: 10.1029/2020jb020270.

Wang, T., Lin, J., Tucholke, B., and Chen, Y. J. Crustal thickness anomalies in the North Atlantic Ocean basin from gravity analysis. *Geochemistry, Geophysics, Geosystems*, 12(3), Mar. 2011. doi: 10.1029/2010gc003402.

Wapenaar, K., Thorbecke, J., and Draganov, D. Relations between reflection and transmission responses of three-dimensional inhomogeneous media. *Geophysical Journal International*, 156 (2):179–194, Feb. 2004. doi: 10.1111/j.1365-246x.2003.02152.x.

Wessel, P., Luis, J. F., Uieda, L. a., Scharroo, R., Wobbe, F., Smith, W. H., and Tian, D. The Generic Mapping Tools Version 6. *Geochemistry, Geophysics, Geosystems*, 20(11):5556–5564, 2019. doi: 10.1029/2019GC008515.

Zelt, B. C. and Ellis, R. M. Receiver-function studies in the Trans-Hudson Orogen, Saskatchewan. *Canadian Journal of Earth Sciences*, 36(4):585–603, Apr. 1999. doi: 10.1139/e98-109.